Optimal High-Frequency Injection Minimizing High-Frequency Torque Ripple for Sensorless Control of Electric Vehicle IPM Traction Motors

Original
Optimal High-Frequency Injection Minimizing High-Frequency Torque Ripple for Sensorless Control of Electric Vehicle IPM Traction Motors / Holczer, A., Freijedo, F.D., Bojoi, R.. - In: IEEE TRANSACTIONS ON INDUSTRIAL ELECTRONICS. - ISSN 0278-0046. - 72:5(2025), pp. 4424-4435. [10.1109/tie.2024.3454189]

Availability:
This version is available at: 11583/2993755 since: 2024-10-27T22:03:16Z

Publisher:
IEEE

Published
DOI:10.1109/tie.2024.3454189

(Article begins on next page)

Optimal High-Frequency Injection Minimizing High-Frequency Torque Ripple for Sensorless Control of Electric Vehicle IPM Traction Motors

András Holczer, *Student Member, IEEE*, Francisco D. Freijedo, *Senior Member, IEEE*, and Radu Bojoi, *Fellow, IEEE*

***Abstract*—A high-frequency (HF) torque ripple-free sinusoidal HF injection-based sensorless control technique is proposed for electric vehicle (EV) traction motors. The sensorless control is developed for interior permanent magnet (IPM) synchronous machines, which is the most commonly used motor type in EV traction applications. The HF torque ripple minimization is performed by injecting sinusoidal voltage along an optimal injection angle in the estimated rotor-aligned dq frame, which varies with the operating point. The magnetic saturation and cross-saturation that affect the operation of most traction motors are properly taken into account. The effectiveness, stability, and parameter sensitivity of the proposed method have been experimentally verified on a commercial 157 kW IPM traction motor mounted on a test rig.**

***Index Terms*—Electric vehicle (EV), high-frequency injection, sensorless control, torque ripple, traction IPMSM.**

I. Introduction

SENSORLESS control of electric drives is undoubtedly one of the most important research topics in the last three decades in the field of motor control and motor design. The main objective of sensorless control is to regulate the speed and torque of electric machines without installing a position sensor on the machine shaft. The literature reports an impressive number of sensorless control solutions, as demonstrated by the numerous survey articles dealing with this topic [1], [2], [3], [4], [5], [6], [7].

The main motivation for sensorless control for industrial applications, such as fans, pumps, compressors, and home appliances, is mostly cost reduction with moderate requirements on torque control quality (bandwidth, torque ripple, and noise). Another reason for removing the position sensor is the drive operation in harsh environments or safety-critical applications, such as aircrafts and very-high speed applications.

Received 18 March 2024; revised 5 June 2024 and 4 August 2024; accepted 25 August 2024. *(Corresponding author: Radu Bojoi.)*

András Holczer and Francisco D. Freijedo are with Nuremberg Research Center, Huawei Technologies Duesseldorf GmbH, 90449 Nuremberg, Germany (e-mail: andras.holczer1@huawei.com; francisco.freijedo@ieee.org).

Radu Bojoi is with Dipartimento Energia, Politecnico di Torino, 10129 Torino, Italy (e-mail: radu.bojoi@polito.it).

Digital Object Identifier 10.1109/TIE.2024.3454189

While the sensorless control has reached a mature level to be put in production for industrial applications and home appliances, the situation is completely different for electrical powertrains employed in electrical vehicles (EVs). Indeed, the EV traction drives require very good torque control quality and accuracy, while keeping the highest possible efficiency [8]. For this reason, a position sensor is always mounted on the motor shaft to ensure high torque control quality. As a result, the main motivation of sensorless control for EV applications is mostly related to safety, as the drive should remain functional in the event of position sensor failure [9], [10]. Hence, sensorless control for EV traction applications increases reliability, and it could have other potential benefits such as cost reduction by using a low-resolution position sensor along with position and speed observer techniques aiming at improving the measurement.

The sensorless control for EV traction drives has been considered [8] as an emerging control solution that must be tailored for the new generations of traction motors. Due to their high torque density, high efficiency, and wide flux-weakening range, interior permanent magnet (IPM) synchronous machines (IPMSMs) fed by three-phase voltage source inverters are widely used today for automotive traction applications [11], [12], [13].

Therefore, the focus of this article is on sensorless control for traction IPM motors employed in EV applications. The literature reports hybrid solutions, where flux or back-electromotive force observers are combined with high-frequency (HF) injection (HFI) [7], [9], [14], [15].

In contrast to the industrial applications, the sensorless control technology for EV traction drives is still under development and validation, due to several challenges resulting from the motor design specifications (deep magnetic saturation and cross-saturation, very low resistance and inductance values), sensing and sampling constraints (open-loop current sensors, single current sampling), control code generation, etc. This statement is justified by the relatively low number of papers reporting experimentally verified sensorless control schemes for torque-controlled traction motors [14], [15], [16]. Indeed, reduced-scale machine prototypes (power levels below 10 kW) may have a different behavior with respect to their full-scale counterparts in terms of inductance values, magnetic saturation, and cross-saturation.

The survey on the recent advances on sensorless control of IPM machines for EV [17] identified the pulsating (or alternating) HF voltage injection as the most promising solution for position estimation at low-speed operation. The pulsating HF injection can be implemented with two main solutions, namely sinusoidal [18] and square wave [19], [20] pulsating HF injection, on the estimated rotor position (d-axis) as standard solution. The first method injects a sinusoidal HF voltage component of frequency that is much lower than the switching frequency (typically below 1 kHz), while the second method injects a square wave HF voltage component at switching frequency or half of switching frequency. The square wave HF injection requires multisampling current acquisition, while sinusoidal HF injection does not [20], since the position and speed estimation relies on current slope and current magnitude measurement, respectively. Therefore, the sinusoidal HF injection is more suitable when single current sampling is preferred, or this is a constraint that is imposed by an existing configuration of the microcontroller employed by the torque control.

This article deals with the sensorless torque control of IPM motors for EV applications, using pulsating sinusoidal HF voltage injection and producing low HF torque ripple. Indeed, as the injected frequency is expected in the range 0.5–1 kHz, the HF torque ripple resulting from the standard HF injection (i.e. on the estimated d-axis) will produce too much noise and vibrations. While this noise may be tolerated for industrial applications, where most of the articles on HFI-based sensorless control focus on signal processing and demodulation techniques, this is not acceptable for electric vehicles [6], [10].

The problem of generating low HF torque ripple is known and it has been considered in the literature, as in [16]. If the HF current vector is tangent to an iso-torque line of the torque map, or, in other words, if it is perpendicular to the maximum torque per ampere (MTPA) current reference trajectory, the resulting HF torque ripple is very small, as proposed [21], [22], [23] for square wave HF injection. The torque ripple is addressed as torque variation in a square-wave injection half-cycle also [24]. A variable amplitude voltage injection is proposed [25] to limit HF current amplitude due to saturation, and torque ripple is decreased with a filtering technique in the current control feedback loop [26]. The above-mentioned solutions reported HF torque ripple reduction for IPM motors and synchronous reluctance motors, leveraging the MTPA current reference trajectory.

The article contributions are summarized as follows:

1) A novel pulsating sinusoidal HF injection scheme with variable dq injection angle is proposed for EV traction IPM motors to minimize the HF torque ripple. By leveraging the knowledge of accurate flux maps that are usually available for the traction motors [17], an optimal dq injection angle is calculated using the flux and incremental inductance values to minimize HF torque ripple for each machine operating point. According to the best knowledge of the authors, this approach is not available in the literature. The proposed approach avoids using the MTPA and iso-torque lines including the MTPA current vector angle as [22], [23] (in [21] the optimal angle is measured via offline experiments, no formulation is provided), thus enabling more flexible application with any current reference strategy.
2) The parameter sensitivity analysis (effects of inductance discrepancy on angle estimation) is carried out and experimentally verified. In the case of HF torque ripple mitigation, the parameter sensitivity increases as pulsating HF voltage vector deviates from the d-axis. This major drawback is not mentioned in the literature [21], [22], [23], [24], [25], [26].
3) The influence of the cross-saturation is taken into account in the formulation of the optimal HF voltage injection angle and in the demodulation scheme, as this influence was not yet considered in the literature [21], [22], [23], [24], [25], [26] for HF torque ripple minimization.

The proposed optimal sinusoidal HF injection has been implemented with conventional field oriented control employing current vector control (CVC-FOC) and it is able to significantly reduce the HF torque ripple, as demonstrated by the experimental verification.

The article is organized as follows: In Section II, the nonlinear IPMSM model is described through the flux maps. Section III proposes a new sinusoidal HF injection technique minimizing the HF torque ripple, along with the proposed demodulation scheme and the analysis on parameter sensitivity. Experimental results on a commercial 157 kW IPMSM are presented in Section IV, validating the proposed method. Section V briefly summarizes the scientific contributions.

II. Nonlinear IPMSM Model

The traction IPM motors are designed to get high torque density with a wide flux-weakening range. Hence, these motors are highly nonlinear, exhibiting deep magnetic saturation, including cross-saturation. To provide accurate torque control, usually through multidimensional look-up tables (LUT) for the generation of torque control references (reference currents or reference flux, depending on the adopted torque control strategy) and also for torque estimation, the motor flux maps must be available, either from calibrated finite-element analysis (FEA) and/or experimental procedures [15], [27], [28]. Recently, the importance of the knowledge of the flux maps for sensorless control has also been clearly emphasized [17].

The machine model is then described as

$$\underline{\Psi}_{dq} = \begin{bmatrix} \Psi_d(\underline{i}_{dq}) \\ \Psi_q(\underline{i}_{dq}) \end{bmatrix} \tag{1a}$$

$$\underline{u}_{dq} = R_s \underline{i}_{dq} + \frac{d}{dt}\underline{\Psi}_{dq} + \mathbf{J}\omega_e \underline{\Psi}_{dq} \tag{1b}$$

$$T_e = \frac{3}{2} p \left(\Psi_d i_q - \Psi_q i_d\right) \tag{1c}$$

where $\underline{\Psi}_{dq} = \begin{bmatrix} \Psi_d & \Psi_q \end{bmatrix}^\top$ is flux vector, $\underline{u}_{dq} = \begin{bmatrix} u_d & u_q \end{bmatrix}^\top$ is voltage vector, $\underline{i}_{dq} = \begin{bmatrix} i_d & i_q \end{bmatrix}^\top$ is current vector, R_s is stator resistance, ω_e is electrical angular speed, T_e is electromagnetic torque, p is pole pair number, and $\mathbf{J} = \mathbf{R}(\pi/2)$ rotation matrix.

The flux maps $\Psi_d(\underline{i}_{dq})$ and $\Psi_q(\underline{i}_{dq})$ are nonlinear functions of i_d and i_q, and furthermore, temperature and rotor position

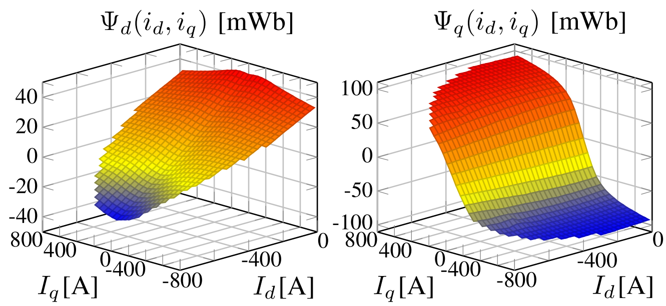

Fig. 1. Direct and quadrature flux maps of the traction IPMSM.

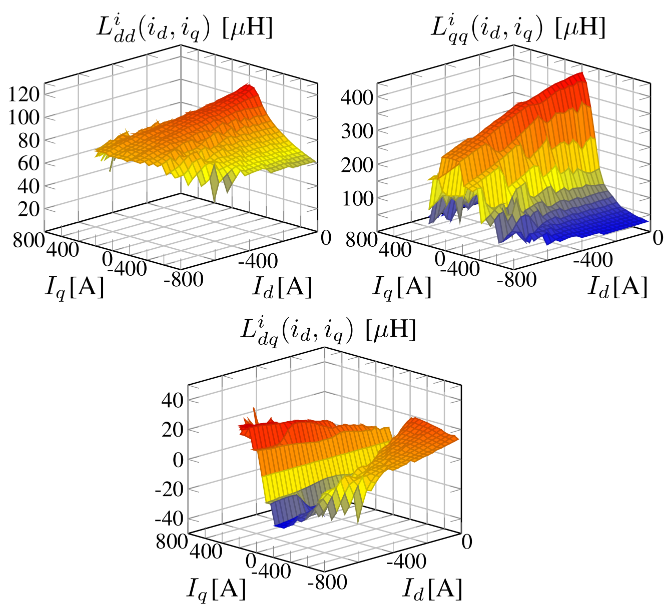

Fig. 2. Incremental inductance maps of the traction IPMSM.

due to spatial flux harmonics affect them [28]. The measured flux maps of the traction machine under test (MUT) (shown in Fig. 7) are depicted in Fig. 1 for half-plane $i_d \leq 0$, since current reference vectors lie in this region.

To linearize the nonlinear plant model about operating points and obtain the incremental inductances, the partial derivatives of the flux maps are calculated as (2)

$$L^i_{dd}(\underline{i}_{dq}) = \frac{\partial \Psi_d(\underline{i}_{dq})}{\partial i_d} \qquad L^i_{qq}(\underline{i}_{dq}) = \frac{\partial \Psi_q(\underline{i}_{dq})}{\partial i_q} \tag{2a}$$

$$L^i_{dq}(\underline{i}_{dq}) = \frac{\partial \Psi_d(\underline{i}_{dq})}{\partial i_q} \qquad L^i_{qd}(\underline{i}_{dq}) = \frac{\partial \Psi_q(\underline{i}_{dq})}{\partial i_d}. \tag{2b}$$

The linearized dq voltage equations yield

$$u_d = R_s i_d + L^i_{dd}(\underline{i}_{dq})\frac{d}{dt}i_d + L^i_{dq}(\underline{i}_{dq})\frac{d}{dt}i_q - \omega_e \Psi_q \tag{3a}$$

$$u_q = R_s i_q + L^i_{qq}(\underline{i}_{dq})\frac{d}{dt}i_q + L^i_{qd}(\underline{i}_{dq})\frac{d}{dt}i_d + \omega_e \Psi_d. \tag{3b}$$

The incremental cross-coupling inductances $L^i_{dq}(\underline{i}_{dq})$ and $L^i_{qd}(\underline{i}_{dq})$ are considered equal [3]. Numerical discrepancy might appear between them when calculated from measured flux maps; thus, the averaged value is depicted in Fig. 2.

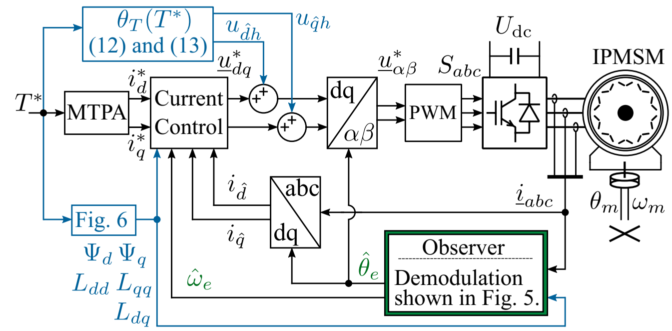

Fig. 3. Block diagram of the proposed sensorless control with HF voltage injection in both d and q axes.

The flux $\Psi_d(\underline{i}_{dq})$, $\Psi_q(\underline{i}_{dq})$ and incremental inductance $L^i_{dd}(\underline{i}_{dq})$, $L^i_{qq}(\underline{i}_{dq})$, $L^i_{dq}(\underline{i}_{dq})$ values depend on dq currents. For the sake of better readability, this dependency is not emphasized below in this article, and incremental inductances are considered if not indicated otherwise.

For saliency-based sensorless control methods, the average and differential inductances are used to analytically derive the system responses. These inductance values are defined as (4), and the saliency ratio is defined as L_{qq}/L_{dd}

$$L_{\text{avg}} = (L_{qq} + L_{dd})/2 \tag{4a}$$

$$L_{\text{diff}} = (L_{qq} - L_{dd})/2. \tag{4b}$$

In the case of IPMSM, the current reference strategy is MTPA to minimize copper losses and inverter conduction losses. The current reference strategy has an influence on the feasible torque range for saliency-based sensorless control since low saliency regions should be avoided to ensure stable angle and speed estimation [10], [28].

Modifying the MTPA current reference may have advantages at low speed, such as a higher saliency ratio and thus more stable HF angle demodulation, with the expense of lower motor efficiency. However, changing the current reference strategy in the transition region between saliency- and model-based methods further complicates the transition [10], [28], [29]. The magnetic characteristics of the machine impose these constraints, hence, flux and incremental inductance maps provide crucial information on the limitations of sensorless control of traction motors.

III. Sensorless Control With Optimal HF Voltage Injection Angle

In the case of sensorless control, the rotor position used for rotational transformations must be estimated by a tracking observer whose inputs are the phase currents, as shown in Fig. 3. The definition of the rotating dq rotor frame is the one used by the surface-mount permanent magnet motors, i.e., the d axis is the position of the magnet flux linkage vector.

The angle error between real and estimated dq frames is defined as $\Delta\theta = \theta_e - \hat{\theta}_e$. The goal of the tracking observer is to drive the $\Delta\theta$ angle error to zero. At zero and low-speed operation, saliency-based methods can provide angle and speed estimation. These methods usually apply additional high-frequency

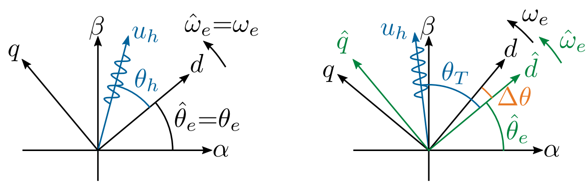

(a) (b)

Fig. 4. Pulsating injection in rotating reference frames. (a) Injection angle θ_h in the real d_q frame. (b) Injection angle θ_T in estimated d_q frame.

voltage injection, and the electrical rotor position and speed are demodulated from HF current responses. Magnetic anisotropy is necessary to identify the rotor position from the HF current. Model-based methods used at middle and high speed [2], [3], [4], [5], [6], [7] are out of the scope of this article.

A. Injection Scheme to Minimize HF Torque Ripple

For IPM motors, the torque is produced as a blend between permanent magnet torque and reluctance torque. When voltage injection is performed, the HF voltage components will create HF current components, and thus HF flux components, according to the machine flux maps. To express the torque ripple, the fundamental current and flux components are separated from the HF components due to HFI. A first-order approximation of flux curves is proposed

$$i_d = i_{d1} + i_{dh} \tag{5a}$$
$$i_q = i_{q1} + i_{qh} \tag{5b}$$
$$\Psi_d = \Psi_{d1} + L_{dd} i_{dh} + L_{dq} i_{qh} \tag{5c}$$
$$\Psi_q = \Psi_{q1} + L_{qq} i_{qh} + L_{dq} i_{dh} \tag{5d}$$

where index 1 means the fundamental components (mostly depending on the torque reference), and index h stands for the HF voltage injection-generated components.

If (5) are used in (1c), and components with the HFI frequency are considered, the torque ripple is given as

$$T_{eh} = 1.5p\Big[(L_{dd} i_{q1} - L_{dq} i_{d1} - \Psi_{q1})\, i_{dh} - (L_{qq} i_{d1} - L_{dq} i_{q1} - \Psi_{d1})\, i_{qh} \Big]. \tag{6}$$

The HF currents depend on the injected HF voltages u_{dh} and u_{qh}. Pulsating injection in dq frame is considered since in this case u_{dh} and u_{qh} are in phase, which ensures that the HF torque ripple consists of a single sinusoidal term, and therefore it is possible to achieve $T_{eh} = 0$. Moreover, in dq frame the rotor position does not affect the condition of $T_{eh} = 0$.

Assuming that the demodulating phase-locked loop (PLL) tracks the electrical angle without error, so $\hat{\theta}_e = \theta_e$, and the injection angle θ_h is measured from the d axis [depicted in Fig. 4(a)], then the dq voltage components are

$$u_{dh} = U_h \cos(\theta_h) \cos(\omega_h t) \tag{7a}$$
$$u_{qh} = U_h \sin(\theta_h) \cos(\omega_h t) \tag{7b}$$

where U_h and ω_h are the amplitude and angular frequency.

To calculate the HF current responses, a purely inductive plant model is considered since the incremental reactance is much bigger than the stator resistance at HFI frequency (Table I). Thus, the HF current components are calculated as

$$\begin{bmatrix} i_{dh} \\ i_{qh} \end{bmatrix} = \begin{bmatrix} L_{dd} & L_{dq} \\ L_{dq} & L_{qq} \end{bmatrix}^{-1} \int \begin{bmatrix} u_{dh} \\ u_{qh} \end{bmatrix} dt \tag{8}$$

$$\begin{bmatrix} i_{dh} \\ i_{qh} \end{bmatrix} = \frac{1}{L_{dd}L_{qq} - L_{dq}^2} \begin{bmatrix} L_{qq} & -L_{dq} \\ -L_{dq} & L_{dd} \end{bmatrix} \int \begin{bmatrix} u_{dh} \\ u_{qh} \end{bmatrix} dt. \tag{9}$$

Hence, the HF dq current components are

$$i_{dh} = A_i [L_{qq} \cos(\theta_h) - L_{dq} \sin(\theta_h)] \sin(\omega_h t) \tag{10a}$$
$$i_{qh} = A_i [L_{dd} \sin(\theta_h) - L_{dq} \cos(\theta_h)] \sin(\omega_h t) \tag{10b}$$
$$A_i = \frac{U_h}{\omega_h} \frac{1}{L_{dd}L_{qq} - L_{dq}^2}. \tag{10c}$$

Substituting (10) into (6) yields the HFI torque ripple as

$$\begin{aligned} T_{eh} = 1.5pA_i \Big[&(L_{dd} i_{q1} - L_{dq} i_{d1} - \Psi_{q1}) L_{qq} \cos(\theta_h) \\ &- (L_{dd} i_{q1} - L_{dq} i_{d1} - \Psi_{q1}) L_{dq} \sin(\theta_h) \\ &- (L_{qq} i_{d1} - L_{dq} i_{q1} - \Psi_{d1}) L_{dd} \sin(\theta_h) \\ &+ (L_{qq} i_{d1} - L_{dq} i_{q1} - \Psi_{d1}) L_{dq} \cos(\theta_h) \Big] \sin(\omega_h t). \end{aligned} \tag{11}$$

The HF electromagnetic torque ripple T_{eh} is a sinusoidal signal whose amplitude depends on the injection angle θ_h. Hence, an injection angle θ_h exists to get $T_{eh} = 0$, i.e.

$$\theta_T = \arctan\left[\frac{\Psi_{q1} L_{qq} + \Psi_{d1} L_{dq} - (L_{dd}L_{qq} - L_{dq}^2) i_{q1}}{\Psi_{d1} L_{dd} + \Psi_{q1} L_{dq} - (L_{dd}L_{qq} - L_{dq}^2) i_{d1}} \right] \tag{12}$$

where θ_T is the optimal value of θ_h in terms of HF torque ripple generation.

The formula has two solutions on $(-180°, 180°]$ with 180° difference. These two solutions describe the same injection with a half-period delay, thus, consider $\theta_T \in (-90°, 90°]$.

Equation (12) proves the existence of an optimal θ_T for any operation condition. For a real-time controller, the solution for each condition is precalculated and stored in a lookup table.

Although the deduction of the optimal injection angle is provided for sinusoidal HF voltage, (12) is valid also for square-wave HF voltage injection. The deduction can be done analogously, following the steps given in Section III-A.

B. High-Frequency Current Response

In the previous section, the optimal injection angle defined in dq frame was calculated to minimize HFI torque ripple, and zero angle error was considered. However, the injection direction can be defined only in the estimated dq frame since the real electrical rotor angle is not known. The demodulation uses $\Delta\theta$ dependent terms of HF current responses in the estimated

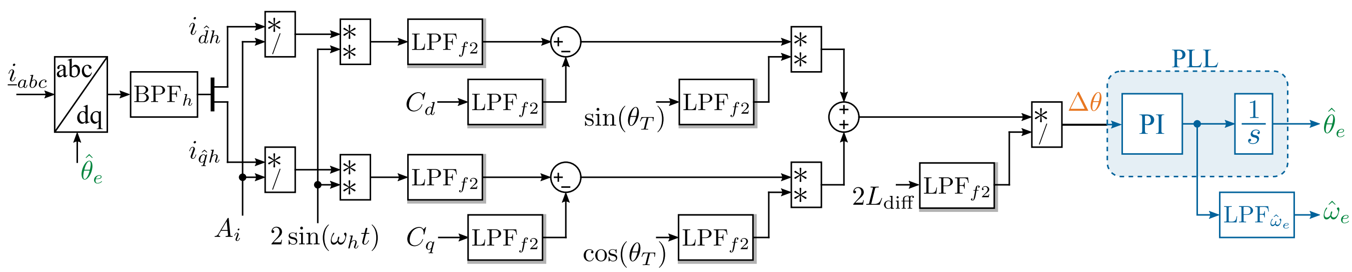

Fig. 5. Demodulation block diagram for torque ripple minimizing HFI using both HF current components.

dq frame as other saliency-based techniques, so the HF currents are expressed in that frame. The injected HF voltages are

$$u_{\hat{d}h} = U_h \cos(\theta_T)\cos(\omega_h t) \tag{13a}$$
$$u_{\hat{q}h} = U_h \sin(\theta_T)\cos(\omega_h t) \tag{13b}$$

which is also shown in Figs. 3 and 4. It translates to

$$u_{dh} = U_h[\cos(\theta_T)\cos(\Delta\theta) + \sin(\theta_T)\sin(\Delta\theta)]\cos(\omega_h t) \tag{14a}$$
$$u_{qh} = U_h[-\cos(\theta_T)\sin(\Delta\theta) + \sin(\theta_T)\cos(\Delta\theta)]\cos(\omega_h t) \tag{14b}$$

in the real dq frame, according to Fig. 4(b).

The HF dq currents can then be calculated as (9)

$$\begin{aligned} i_{dh} = A_i\Big[&L_{qq}(\cos(\theta_T)\cos(\Delta\theta) + \sin(\theta_T)\sin(\Delta\theta)) \\ &- L_{dq}(-\cos(\theta_T)\sin(\Delta\theta) + \sin(\theta_T)\cos(\Delta\theta))\Big]\sin(\omega_h t) \end{aligned} \tag{15a}$$
$$\begin{aligned} i_{qh} = A_i\Big[&-L_{dq}(\cos(\theta_T)\cos(\Delta\theta) + \sin(\theta_T)\sin(\Delta\theta)) \\ &+ L_{dd}(-\cos(\theta_T)\sin(\Delta\theta) + \sin(\theta_T)\cos(\Delta\theta))\Big]\sin(\omega_h t). \end{aligned} \tag{15b}$$

The demodulation uses currents in the estimated dq frame, these current components can be computed as

$$i_{\hat{d}h} = i_{dh}\cos(\Delta\theta) - i_{qh}\sin(\Delta\theta) \tag{16a}$$
$$i_{\hat{q}h} = i_{dh}\sin(\Delta\theta) + i_{qh}\cos(\Delta\theta). \tag{16b}$$

From (15) and (16), and applying trigonometric identities, the current responses are

$$\begin{aligned} i_{\hat{d}h} = A_i\Big[&(L_{\text{avg}} + L_{\text{diff}}\cos(2\Delta\theta))\cos(\theta_T) \\ &+ L_{\text{diff}}\sin(2\Delta\theta)\sin(\theta_T) \\ &+ L_{dq}(\sin(2\Delta\theta)\cos(\theta_T) - \cos(2\Delta\theta)\sin(\theta_T))\Big]\sin(\omega_h t) \end{aligned} \tag{17a}$$
$$\begin{aligned} i_{\hat{q}h} = A_i\Big[&L_{\text{diff}}\sin(2\Delta\theta)\cos(\theta_T) \\ &+ (L_{\text{avg}} - L_{\text{diff}}\cos(2\Delta\theta))\sin(\theta_T) \\ &- L_{dq}(\sin(2\Delta\theta)\sin(\theta_T) + \cos(2\Delta\theta)\cos(\theta_T))\Big]\sin(\omega_h t). \end{aligned} \tag{17b}$$

Both HF current responses in the estimated dq frame contain information of $\Delta\theta$, hence, a demodulation strategy is proposed that uses both HF current components to calculate $\Delta\theta$ and to provide an estimation of electrical speed and rotor position.

C. Demodulation Scheme in Tracking Position Observer

The sensorless angle and speed observer relies on the HF current components in the estimated dq frame, hence, they are filtered from the fundamental ones with a band-pass filter tuned to injection frequency (BPF$_h$), as shown in Fig. 5. The BPF$_h$ consists of a second-order low- and high-pass filter with cutoff frequency ω_h, thus, no phase delay is imposed, and signal amplitude at ω_h frequency is not influenced either.

In the case of pulsating HF voltage injection, the HF current response is amplitude modulated by $\Delta\theta$. After amplitude normalization by A_i, the HF current components are multiplied by a sinusoidal signal with identical frequency and then filtered with a second-order low-pass filter (LPF$_{f2}$) to remove the double frequency component and obtain the amplitude of interest. This method is explained by

$$A\sin(\omega_h t + \varphi)2\sin(\omega_h t) = A(\cos(\varphi) - \cos(2\omega_h t + \varphi)) \tag{18}$$

where A is the amplitude of interest, and φ is the possible phase discrepancy due to the resistive part, and other nonideal factors in the demodulation scheme, which is small and therefore $\cos(\varphi)$ has a very small effect on the amplitude. The 1.5 sampling time delay that is present in most real-time systems with sampled feedback is taken into account by phase advancing the HF voltage reference.

Since the PLL in the demodulation scheme drives $\Delta\theta$ close to 0, $\cos(2\Delta\theta) \approx 1$ and $\sin(2\Delta\theta) \approx 2\Delta\theta$, the HF current components are approximated from (17) as

$$\begin{aligned} i_{\hat{d}h} \approx A_i\Big[&(L_{qq}\cos(\theta_T) - L_{dq}\sin(\theta_T)) \\ &+ (2L_{\text{diff}}\sin(\theta_T) + 2L_{dq}\cos(\theta_T))\Delta\theta\Big]\sin(\omega_h t) \end{aligned} \tag{19a}$$
$$\begin{aligned} i_{\hat{q}h} \approx A_i\Big[&(L_{dd}\sin(\theta_T) - L_{dq}\cos(\theta_T)) \\ &+ (2L_{\text{diff}}\cos(\theta_T) - 2L_{dq}\sin(\theta_T))\Delta\theta\Big]\sin(\omega_h t). \end{aligned} \tag{19b}$$

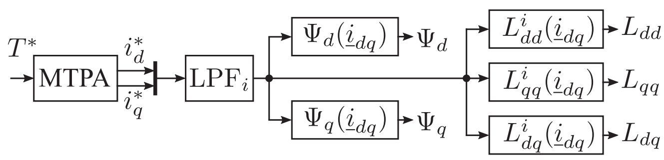

Fig. 6. Evaluation of flux and incremental inductance maps.

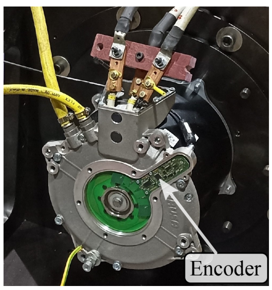

Fig. 7. Picture of MUT.

TABLE 1
RATED DATA OF MUT

Peak Power	157 kW
Torque	150 Nm
Speed	4900 rpm
DC voltage	400 V
Current	230 A_{eff}
Pole pairs	5
R_s @ 25 °C	9 mΩ
Ψ_{PM}	42 mWb
L_{dd}	92 μH
L_{qq}	332 μH

These linearized formulas are considered in the parametrization of the demodulation block. The intervals of initial convergence and polarity detection can be analyzed separately.

The proposed demodulation is shown in Fig. 5, where

$$A_i = \frac{U_h}{\omega_h}\frac{1}{L_{dd}L_{qq} - L_{dq}^2} \tag{20a}$$

$$C_d = L_{qq}\cos(\theta_T) - L_{dq}\sin(\theta_T) \tag{20b}$$

$$C_q = L_{dd}\sin(\theta_T) - L_{dq}\cos(\theta_T) \tag{20c}$$

using operating point-dependent parameters. These values are obtained by evaluating the flux and incremental inductance map lookup tables (LUTs) using filtered current reference values, as shown in Fig. 6. Reference values are used to avoid measurement noise and transients; the first-order LPF_i approximates closed-loop current control.

In the demodulation scheme, after removing the double frequency component with LPF_{f2}, $\Delta\theta$ dependent and $\Delta\theta$ independent terms are acquired. To obtain only $\Delta\theta$ dependent term at the PLL input, the $\Delta\theta$ independent terms are subtracted; these expressions are given as (20b) and (20c). C_d and C_q are filtered with the same LPF_{f2} to synchronize the signals

$$\begin{aligned} 2L_{\text{diff}}\Delta\theta &= \sin(\theta_T)(2L_{\text{diff}}\sin(\theta_T) + 2L_{dq}\cos(\theta_T))\Delta\theta \\ &\quad + \cos(\theta_T)(2L_{\text{diff}}\cos(\theta_T) - 2L_{dq}\sin(\theta_T))\Delta\theta. \end{aligned} \tag{21}$$

Then the d branch is multiplied by $\sin(\theta_T)$, the q branch is multiplied by $\cos(\theta_T)$ and they are added to eliminate L_{dq} in the coefficient of $\Delta\theta$ as shown (21). In this way, the resultant coefficient of $\Delta\theta$ is $2L_{\text{diff}}$. Then division by $2L_{\text{diff}}$ is applied to obtain normalized angle error as input for the tracking PLL.

Expressions $\sin(\theta_T)$, $\cos(\theta_T)$, and $2L_{\text{diff}}$ are also filtered with LPF_{f2} to synchronize the time delay in all parallel branches of the demodulation and therefore to decrease the angle error in transients where θ_T changes intensively.

After $\Delta\theta$ is obtained, it serves as input for the tracking PLL, which consists of a PI block and an integrator. This structure is widely discussed in the literature [30], [31].

The demodulation involves digital band-pass and low-pass filtering and integration, which effectively mitigates current measurement additive white noise due to current sensor characteristics and digital acquisition. Hence, the electrical position and speed estimation are reliable from current measurement quality point of view [32].

D. Parameter Sensitivity

The obvious advantage of the proposed injection scheme and demodulation is the significantly reduced torque ripple compared with injection in the estimated d direction. The maximum bandwidths of the two methods are similar; the main disadvantage of the torque ripple-free method is the sensitivity of angle estimation to inductance variation in steady-state angle tracking, which is analyzed in this section. If the compensation of $\Delta\theta$ independent terms is not perfect, there will be a steady-state angle error $\Delta\theta_{ss}$, since the PLL drives its input to zero, and consequently it creates $\Delta\theta_{ss} \neq 0$.

If the incremental inductance parameters used for the demodulation do not exactly match the machine parameters, the $\Delta\theta$ independent parts are not compensated perfectly, and the remaining value causes angle estimation error since the PLL drives its input to zero, but this input does not include only $\Delta\theta$ dependent values. If the machine and control parameters are indicated by superscripts ^{m} and ^{c}, respectively, and assuming a small $\Delta\theta$, the steady-state angle error is

$$\begin{aligned} \Delta\theta_{ss} = \frac{1}{2L^m_{\text{diff}}}\frac{A^c_i}{A^m_i}\Bigg[&\left(\frac{A^m_i}{A^c_i}L^m_{dq} - L^c_{dq}\right) \\ &-\left(\frac{A^m_i}{A^c_i}L^m_{qq} - L^c_{qq} + \frac{A^m_i}{A^c_i}L^m_{dd} - L^c_{dd}\right)\cos(\theta_T)\sin(\theta_T)\Bigg] \end{aligned} \tag{22a}$$

where

$$\frac{A^m_i}{A^c_i} = \frac{L^c_{dd}L^c_{qq} - L^c_{dq}L^c_{dq}}{L^m_{dd}L^m_{qq} - L^m_{dq}L^m_{dq}}. \tag{22b}$$

The machine parameters cannot be identified without measurement uncertainty; they vary with temperature and shift over time, hence $\Delta\theta_{ss} \neq 0$ is expected.

In the case of $\theta_T = 0$ (d injection), only the uncertainty of L_{dq} affects $\Delta\theta_{ss}$. Since L_{dq} is much smaller than L_{dd} and L_{qq}, injection into the d direction is less affected by parameter uncertainty than injection into the torque ripple minimizing direction. For instance, if 10% inductance error is considered with $T^* = 50$ Nm MTPA current references, $\Delta\theta_{ss} = -4.8°$, while for standard d injection it is only $\Delta\theta^d_{ss} = 0.2°$. The increased parameter sensitivity was experimentally verified (including the previous numerical values), which is detailed in Section IV-B. It shows that using accurate inductance maps is key for this method. Traction IPM motors are well known and properly characterized using experimental procedures to obtain the flux maps, and therefore the inductance maps are usually available with good accuracy. Hence, applying the proposed method to EV traction IPM motors is possible.

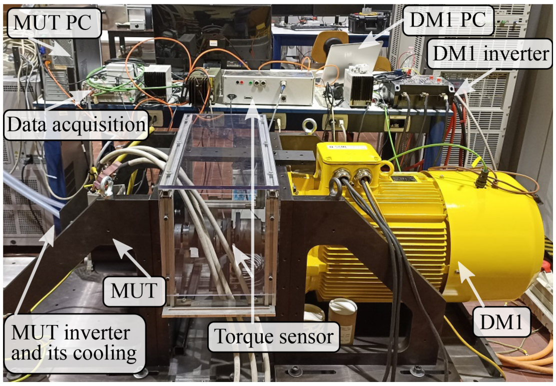

Fig. 8. Test rig of 157 kW EV traction IPMSM with speed-controlled synchronous reluctance driving machine.

IV. Experimental Verification

The proposed sensorless control, including HF injection and demodulation schemes, has been experimentally validated on a commercial liquid-cooled 157 kW traction IPMSM manufactured by BRUSA (parameters listed in Table I) and mounted on two test rigs with speed-controlled driving machines, as shown in Figs. 8 and 11. The first driving machine (DM1) was a 45 kW 430 Nm synchronous reluctance motor, while the second driving machine (DM2) was a 22 kW 100 Nm induction motor (IM). The IPM motor is equipped with a low-resolution position sensor designed for traction, with 480 pulses per mechanical revolution, which translates to 3.75° resolution in the electrical domain. The real-time sensorless control has been implemented in C language on a dSPACE MicroLabBox platform operated by ControlDesk, using a sampling frequency of $f_s = 10$ kHz. The IPM motor was fed by an OnSemi NVG800A75L4DSC-EVK inverter with $f_{sw} = 10$ kHz switching frequency. The IGBTs are rated at 800 A 750 V, and phase currents were measured with built-in current sensors. The inverter nonlinearities (dead-time effects and resistive voltage drop on semiconductor devices) were compensated in an experimentally identified LUT-based feedforward manner [33]. The torque control is realized by open-loop torque reference to current reference MTPA LUTs evaluation, and closed-loop current control is achieved using the estimated electrical angle and speed, as shown in Fig. 3. HBM T40B torque sensors were used to validate torque control and torque estimation formula.

The HF voltage injection amplitude was $U_h = 20$ V, and the injection frequency was $f_h = 500$ Hz ($\omega_h = 3141.6$ rad/s). The injection frequency is limited by the switching and sampling frequency, and the injection frequency limits the observer bandwidth, which sets a limit to the current control bandwidth. In this case study, the closed-loop current control bandwidth was set to 100 Hz (628.3 rad/s), able to track current references generated by torque reference with 500 Nm/s slew rate limit. It means that 100 Nm torque is achieved in 200 ms, which is reasonable dynamics for a vehicle traction drive that works in a faulty condition (damaged position sensor), and obviously the dynamic performance has to be limited.

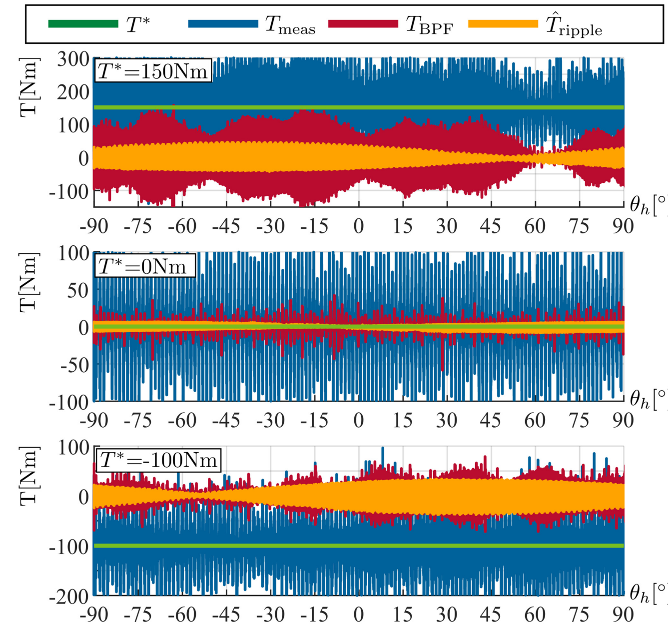

Fig. 9. Reference torque, measured torque, band-pass filtered, and estimated torque ripple for different torque references.

A. Optimal Injection Angle

To experimentally verify the proposed analytical formulation of the optimal HF voltage injection angle (12), the HF torque ripple was measured in the case of pulsating HF voltage injection in real dq frame with sweeping injection angle (with $U_h = 25$ V only for this test case). The test was carried out on a high-torque test rig shown in Fig. 8, as the high moment of inertia of DM1 (0.5 kgm^2) made torque ripple measurement possible. The results are shown in Fig. 9, where T^* is the torque reference, T_{meas} is the measured torque provided by the torque sensor, T_{BPF} is the output of a fourth-order digital band-pass filter with T_{meas} input (tuned to the HF injection frequency to obtain the HF torque ripple), and $\hat{T}_{\text{ripple}}$ is the estimated torque ripple. Estimating the torque and torque ripple of MUT was necessary since the torque sensor with 1000 Nm range provided a very noisy signal, especially at high torque values, which could be imposed by the accuracy of the torque sensor, by the shaft coupler placed between the MUT and the torque sensor, or by the speed-controlled DM1.

To mitigate the uncertainty of the torque ripple and consequently the optimal injection angle measurement, torque ripple estimation was implemented in the real dq frame with the following equations:

$$\hat{T} = \frac{3}{2}p\left(\Psi_d(i_d, i_q)i_q - \Psi_q(i_d, i_q)i_d\right) \tag{23}$$

$$\hat{T}_{\text{ripple}} = \hat{T} - T^*. \tag{24}$$

It is underlined that the estimated torque ripple (24) is used for verification only and not for control purposes. The measured optimal injection angle θ_{meas} was determined from the estimated

TABLE II
ANALYTICAL AND MEASUREMENT RESULTS FOR OPTIMAL INJECTION ANGLE FOR TORQUE RIPPLE MINIMIZATION

T^* [Nm]	θ_{meas} [°]	θ_T [°]	T^* [Nm]	θ_{meas} [°]	θ_T [°]
−150	(−54,−47)	−52.2	150	(47,53)	52.2
−140	(−54,−48)	−51.9	140	(47,53)	51.9
−130	(−58,−52)	−56.1	130	(50,58)	56.1
−120	(−56,−50)	−54.9	120	(48,55)	54.9
−110	(−57,−51)	−55.8	110	(48,58)	55.8
−100	(−60,−52)	−56.7	100	(49,59)	56.7
−90	(−59,−53)	−56.5	90	(48,58)	56.5
−80	(−60,−54)	−57.4	80	(51,60)	57.4
−70	(−59,−52)	−55.7	70	(52,60)	55.7
−60	(−60,−50)	−58.8	60	(52,60)	58.5
−50	(−61,−53)	−56.9	50	(51,60)	56.9
−40	(−60,−51)	−58.0	40	(51,59)	58.0
−30	(−58,−51)	−55.2	30	(48,58)	55.2
−20	(−53,−46)	−50.2	20	(42,49)	50.2
−15	(−48,−41)	−44.7	15	(34,44)	44.7
−10	(−41,−32)	−36.7	10	(22,32)	36.7
−5	(−30,−20)	−20.5	5	(4,13)	20.5
0	(−12, −4)	0.0	0.0	(−12,−4)	0.0

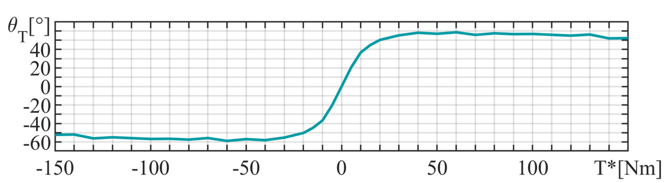

Fig. 10. Optimal injection angle (θ_T) as the function of T^*.

torque ripple signal, since it was less affected by noise than the torque sensor signal. Even the torque ripple estimation involves noise due to position sensor resolution and current measurement uncertainty, and therefore, measured optimal angle intervals are indicated in Table II instead of single values. The theoretical optimal angle θ_T is calculated as (12) (listed in Table II) using the measured flux maps and the derived incremental inductance maps, and $\theta_T(T^*)$ is plotted in Fig. 10. The calculated optimal angle matches well with the measured results, which validates the analytical formulation of the optimal injection angle given as (12). There is some discrepancy at low torque values, where the torque ripple is the smallest (Fig. 9), thus the results are the most affected by measurement inaccuracies. The flux maps of an IPMSM are symmetric to $I_q = 0A$ axis, hence $\theta_T(T^*)$ is and odd function, which is theoretically proven by (12). Hence, at low torque, the theoretical values are trusted more than the measured ones.

It can be seen on the estimated torque ripple signal in Fig. 9 that the amplitude of the HF torque component is a sinusoidal function of the injection angle θ_h. This property can be concluded from (11) since the amplitude of the sinusoidal HF torque consists of a linear combination of $\sin(\theta_h)$ and $\cos(\theta_h)$, which can be written as a single sine function with phase offset that would correspond to the optimal injection angle to minimize HF torque ripple.

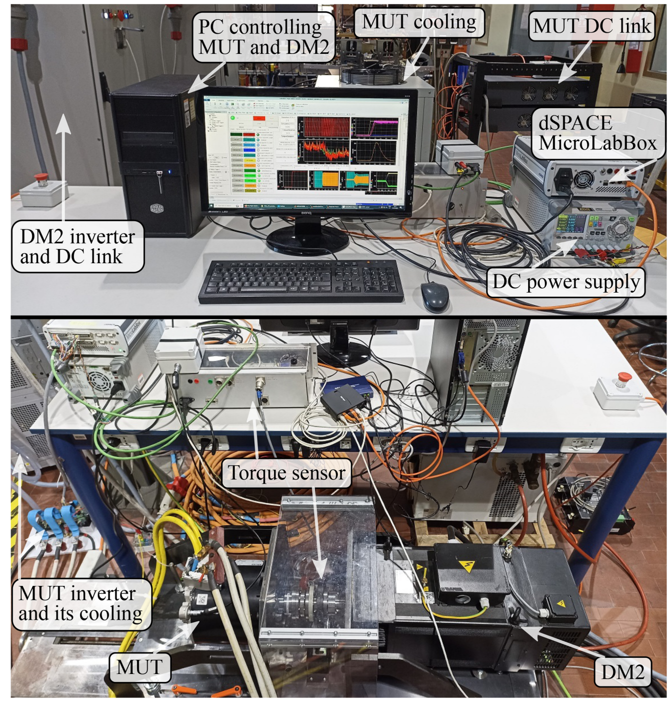

Fig. 11. Test rig of the MUT with speed-controlled IM DM.

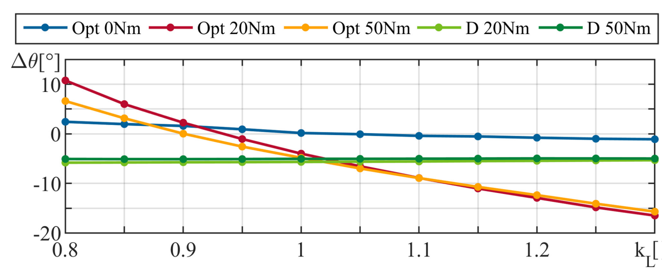

Fig. 12. Angle error caused by inductance discrepancy.

B. Parameter Sensitivity in Steady-State Operation

As shown analytically in Section III-D, the parameter sensitivity increases with the HF torque ripple minimizing injection scheme. In order to experimentally verify (22), parameter mismatch was imposed as $L^c = k_L L^m$ for all inductances. The angle error deviation caused by inductance discrepancy was tested for d and optimal injection on the test rig shown in Fig. 11 for 0, 20, and 50 Nm torque references in steady-state operation at 240 rpm. The averaged angle errors for 20 electrical periods are plotted in Fig. 12. In the case of d injection, k_L has very little effect on $\Delta\theta$, however, in the case of the optimal injection $\Delta\theta$ varies significantly with k_L. The results match very well with the numerical values elaborated in Section III-D: approximately 5° angle error is caused by 10% inductance variation. The parameter sensitivity is higher at 20 Nm ($\theta_T = 50.2°$) than at 50 Nm ($\theta_T = 56.9°$), as predicted by (22). In conclusion, the inductance values have to be known precisely to apply the HF

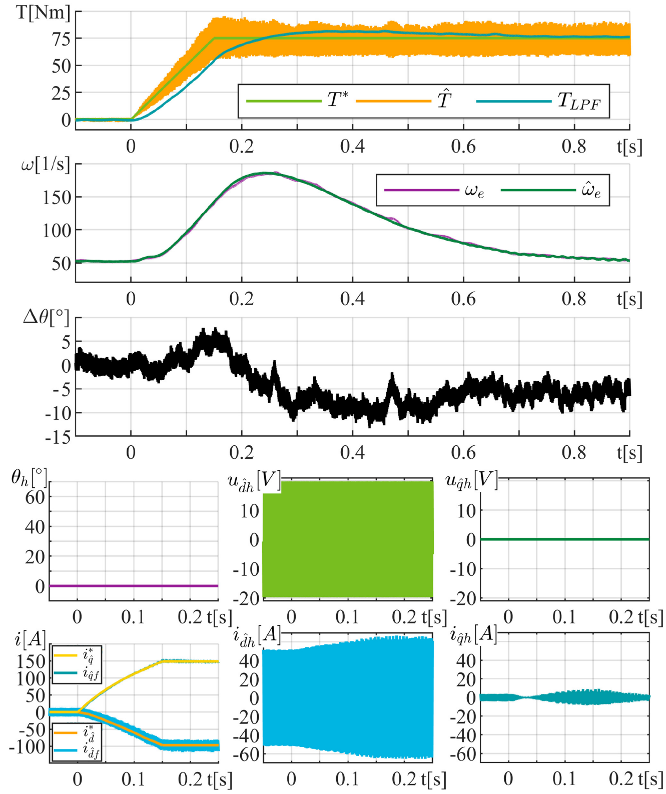

Fig. 13. Torque transient with d HF injection scheme.

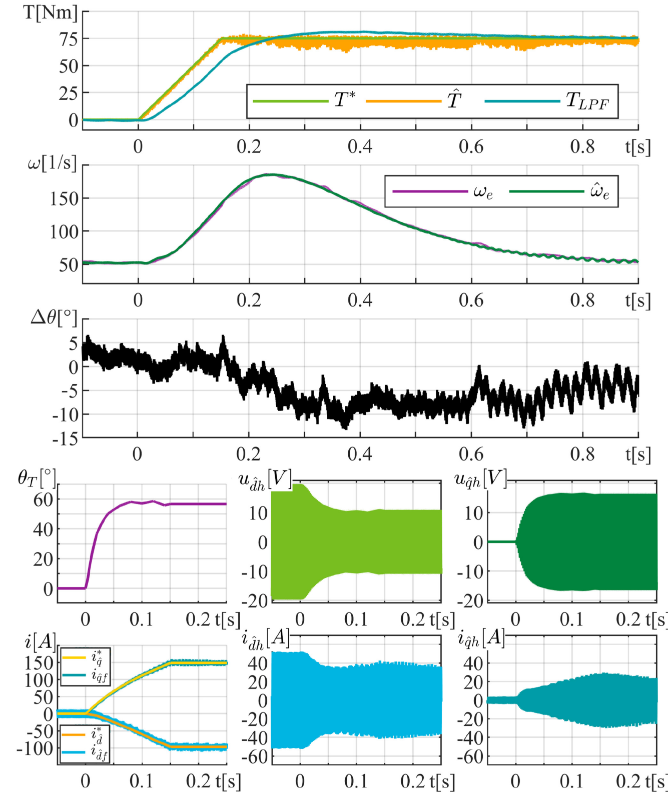

Fig. 14. Torque transient with optimal HF injection scheme.

torque ripple minimization injection. However, this is not critical for traction motors, as they are always well characterized from the point of view of their magnetic model. Stability of the HF torque ripple minimizing sensorless control is not ensured if constant inductance values are used due to the lack of proper nonlinear characterization.

C. Torque Transients in Sensorless Mode

Variation of the injection angle imposes challenges for the demodulation scheme and for the angle tracking observer. Torque transients from zero to positive torque are analyzed in Figs. 13 and 14 representing an acceleration transient of the car. In these transient plots, the low-pass filtered measured torque (T_{LPF}) is indicated to filter the very noisy torque sensor signal, and to show the torque between the machines that generate the mechanical transient. The estimated torque of MUT is also depicted to show torque control performance and the estimated torque ripple. Experimental results are obtained on the test rig with DM2 shown in Fig. 11, with HBM T40B torque sensor with 200 Nm range.

It can be seen in Figs. 13 and 14 that the improvement of the proposed injection scheme, namely torque ripple reduction for all torque references, is significant, which is achieved by varying the HF voltage injection angle according to the torque reference. Some torque ripple can be observed in Fig. 14 which is caused mainly by the angle error, as injection is defined in the estimated dq frame. A clearer comparison is provided when the optimal injection is switched to d injection at 75 Nm,

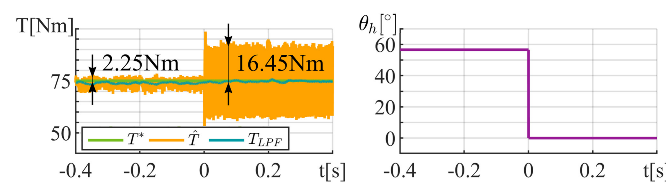

Fig. 15. Switching between optimal and d voltage injection.

which is shown in Fig. 15. The averaged peak-to-peak estimated torque value for 100 HF periods increases from 4.5 to 32.9 Nm when d injection is activated. It means that the optimal injection scheme reduces the torque ripple from 16.45 to 2.25 Nm (from 11.0% to 1.5% of the rated torque). The injection angle θ_T is measured from the estimated d axis, hence, if angle error is not negligible, some torque ripple will be generated since the injection does not happen in optimal direction in the real dq frame. However, it will still be much lower than in the case of standard d injection. If the angle error was calibrated to zero by a LUT-based compensation, the torque ripple would decrease even more. For the results presented in this article, no calibration and LUT-based angle error compensation took place to intentionally show the effect of parameter sensitivity, which is the other main aspect of the proposed control.

Although the flux maps are measured and inductance maps are derived from them, the parameters used in control do not exactly match the machine parameters due to limited measurement accuracy. The effect of parameter sensitivity issues can

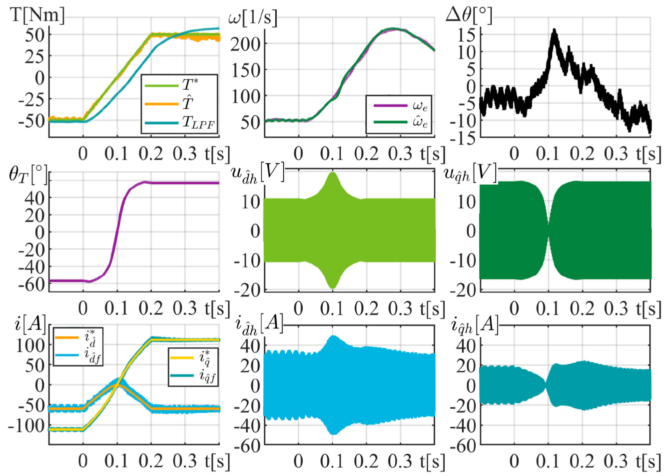

Fig. 16. Symmetrical torque transient with optimal HF injection scheme.

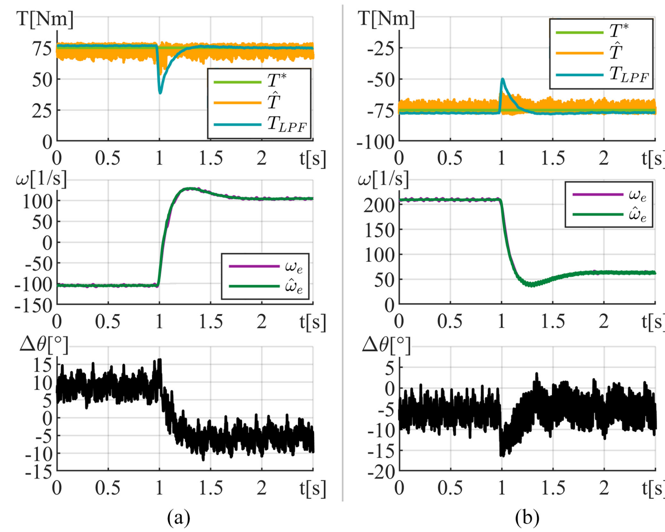

Fig. 17. Speed transient with optimal HF injection scheme. (a) Acceleration from -200 rpm to 200 rpm with 75 Nm MUT torque. (b) Deceleration from 400 rpm to 120 rpm with -75 Nm MUT torque.

be observed by comparing angle error plots in Figs. 13 and 14. The angle error is slightly higher in the case of torque ripple minimizing injection scheme, and it undergoes higher oscillation when the torque is constant. It shows the clear effect of increased parameter sensitivity, by using only nominal constant parameters, the sensorless angle and speed observer would easily fail with increasing torque.

In both cases, the current control in the estimated dq frame achieves accurate current, and consequently torque control. Since $L_{qq} > L_{dd}$, the HF current amplitude is smaller in the case of optimal injection, hence the generated loss decreases.

The objective of symmetrical torque transients is to analyze the stability of the sensorless observer when the injection angle variation is the highest: -50 to 50 Nm torque transient is presented in Fig. 16. The same torque slew rate is applied as before in order not to compromise the dynamics of the drive when the torque reference sign changes. The HF torque ripple is effectively eliminated for both negative and positive torque values. The injection angle changes from $-58°$ to $58°$ when torque reference changes from -40 to 40 Nm which corresponds to (0.02 s, 0.18 s) time interval in Fig. 16.

In this transient, the angle error is expected to be the highest since the HF voltages vary intensively as shown in Fig. 16. The maximum value of angle error is around $14°$ (averaged value due to low encoder resolution), which is an acceptable angle error, and it lasts only for a short time. The moment of inertia of DM2 was very low (0.075 kgm^2) compared with the apparent moment of inertia that would correspond to the weight of an EV. Although the DM2 was speed controlled, the shaft underwent intensive speed transient that negatively affected the angle estimation, demonstrating the robustness of the sensorless control against fast speed and torque transients. The peak acceleration shown in Fig. 16 in electrical domain was approximately 1000 rad/s^2 that is equivalent to 1910 rpm/s acceleration in mechanical domain, which is quite a high value for 100 Nm torque reference variation. Hence, smaller angle error peak would be expected if the method was tested on an electric vehicle.

Once the torque reference reaches 50 Nm, the angle error converges back to its steady-state value and the proposed sensorless control works as well as with d injection in terms of angle estimation. However, in terms of torque ripple, the improvement is significant, as described in detail in this article. Even in worst-case torque transients, the sensorless angle and speed estimation are stable and provide reliable current control in the estimated dq frame without applying any offline angle estimation calibration. If LUT-based calibration algorithm had been applied utilizing the encoder signal, a lower angle error would have been obtained. The overall effect of non-negligible angle error is the slightly decreased machine torque, since the current vector in real dq frame is rotated by $\Delta\theta$ from the MTPA current vector.

D. Speed Transients in Sensorless Mode

In order to test the effects of external disturbance on the proposed sensorless control, speed transients were imposed by the speed reference variation of DM2 at constant torque of the MUT. An acceleration transient with speed reversal for positive torque is shown in Fig. 17(a), and a deceleration transient with negative torque is shown in Fig. 17(b). Internal electrical variables related to HFI and current control of the MUT are not detailed as they do not vary. The shaft acceleration was even higher in this case than in the case of the elaborated symmetrical torque transient. This fast acceleration caused a maximum $7°$ angle error variation, which shows very good tracking ability of the angle demodulation for speed transients caused by external disturbances. The high pole pair number is disadvantageous as the external load disturbance caused by mechanical transient is amplified in electrical domain. Although EV traction motors have high pole pair number, fast motor speed transient caused by external factors cannot be expected, thus the angle estimation will not be compromised.

The sensorless control proved to be stable in the case of torque transients up to 100 Nm torque reference variation from -100 to 100 Nm with different mechanical speeds from -1000 to 1000 rpm; and also in the case of external disturbance caused speed transients, including speed reversals. Over 10% of the nominal speed (4900 rpm), model-based methods take over angle and speed estimation. The proposed method was verified to be stable on a much wider speed range than necessary for application in an EV traction drive. The overall maximum absolute value of angle error was 15°. The steady-state angle estimation oscillation intensified above 100 Nm (and under -100 Nm). Angle estimation oscillation could be reduced by reducing the angle and speed tracking PLL bandwidth, but it resulted in higher angle error for torque and speed transients due to slower angle tracking. The optimal value selection is an engineering trade-off between fast angle tracking and noise mitigation.

As a general conclusion of the experimental verification, the proposed injection scheme significantly reduces the torque ripple generated by the high-frequency voltage injection and provides almost as good angle estimation as the standard injection in d direction if the incremental inductance values are precisely known.

V. Conclusion

In this article, a high-frequency torque ripple minimizing sinusoidal voltage injection technique and its demodulation scheme is proposed. This method produces a very small torque ripple, as demonstrated by the experimental verification. One aspect of the sensorless control of EV traction drives is maintaining high torque quality, and therefore, the elimination of the HF torque ripple by optimal injection is a significant contribution to quality improvement compared to the standard d pulsating injection scheme. The variation of the optimal injection angle as a function of the torque reference is addressed in this article both in terms of analytical deduction and experimental verification. The proposed methodology for the calculation of the optimal injection angle has a high degree of generality, and therefore it can be applied to other sensorless techniques using HF injection. The adopted sensorless technique for this work was sinusoidal HF injection due to the limitation of the single current sampling.

As another important contribution, the parameter sensitivity is analytically expressed and experimentally verified. The main drawback of deviating the pulsating HF voltage injection from the d direction is the increased parameter sensitivity on the estimated angle, which was not shown before.

The control is validated for torque and speed transient scenarios on a commercial traction IPMSM mounted on test rigs. The torque ripple is effectively mitigated, and with this, the vibration and HF noise of the drive are avoided. The proposed method depends on the knowledge of motor inductance maps, which are usually well known for traction motors. The angle error remains within the (–15°,15°) interval (without any angle estimation calibration), even with the worst-case symmetrical torque transient, hence, the proposed control is stable and can be applied in an EV traction drive.

References

[1] P. P. Acarnley and J. F. Watson, "Review of position-sensorless operation of brushless permanent-magnet machines," *IEEE Trans. Ind. Electron.*, vol. 53, no. 2, pp. 352–362, 2006.

[2] S. Kim and S.-K. Sul, "Sensorless control of AC motor — Where are we now?" in *Proc. Int. Conf. Elect. Mach. Syst.*, 2011.

[3] R. Bojoi, M. Pastorelli, J. Bottomley, P. Giangrande, and C. Gerada, "Sensorless control of PM motor drives - A technology status review," in *Proc. IEEE Workshop Elect. Mach. Des., Control Diagnosis (WEMDCD)*, Paris: IEEE Press, 2013, pp. 168–182.

[4] Y. Kano and N. Matsui, "Sensorless control of interior permanent magnet synchronous motor: An overview and design study," in *Proc. IEEE Workshop Elect. Mach. Des., Control Diagnosis (WEMDCD)*, Nottingham, United Kingdom: IEEE Press, 2017, pp. 199–207.

[5] S.-K. Sul, Y.-C. Kwon, and Y. Lee, "Sensorless control of IPMSM for last 10 years and next 5 years," *CES Trans. Elect. Machin. Syst.*, vol. 1, no. 2, pp. 91–99, 2017.

[6] G. Wang, M. Valla, and J. Solsona, "Position Sensorless Permanent Magnet Synchronous Machine Drives—A Review," *IEEE Trans. Ind. Electron.*, vol. 67, no. 7, pp. 5830–5842, Jul. 2020.

[7] Z. Zhang, "Sensorless back EMF based control of synchronous pm and reluctance motor drives—a review," *IEEE Trans. Power Electron.*, vol. 37, no. 9, pp. 10290–10305, Sep. 2022.

[8] C. Liu, K. T. Chau, C. H. T. Lee, and Z. Song, "A critical review of advanced electric machines and control strategies for electric vehicles," *Proc. IEEE*, vol. 109, no. 6, pp. 1004–1028, Jun. 2021.

[9] N. Patel, T. O'Meara, J. Nagashima, and R. Lorenz, "Encoderless IPM traction drive for EV/HEV's," in *Proc. IEEE Ind. Appl. Conf., 36th IAS Annu. Meeting*. Piscataway, NJ, USA: IEEE Press, 2001.

[10] A. Holczer, F. D. Freijedo, and R. Bojoi, "Overview of sensorless control strategies for electric vehicle traction ipmsm," in *Proc. IEEE Workshop Elect. Mach. Des., Control Diagnosis*, 2023.

[11] A. M. El-Refaie, "Motors/generators for traction/propulsion applications: A review," *IEEE Veh. Technol. Mag.*, vol. 8, no. 1, pp. 90–99, Mar. 2013.

[12] P. Ramesh and N. C. Lenin, "High power density electrical machines for electric vehicles—Comprehensive review based on material technology," *IEEE Trans. Magn.*, vol. 55, no. 11, pp. 1–21, Nov. 2019.

[13] E. Agamloh, A. von Jouanne, and A. Yokochi, "An Overview of electric machine trends in modern electric vehicles," *Machines*, vol. 8, no. 2, 2020, Art. no. 20.

[14] J. Lara, A. Chandra, and J. Xu, "Integration of HFSI and extended-EMF based techniques for PMSM sensorless control in HEV/EV applications," in *Proc. 38th Annu. Conf. IEEE Ind. Electron. Soc.*, Montreal, QC, Canada, 2012.

[15] W. Zine et al., "Compensation of cross-saturation effects on IPMSM sensorless control - application to electric vehicle," in *Proc. Annu. Conf. IEEE Ind. Electron. Soc.*, 2016.

[16] J. Lara and A. Chandra, "Performance investigation of two novel HSFSI demodulation algorithms for encoderless FOC of PMSMs intended for EV propulsion," *IEEE Trans. Ind. Electron.*, vol. 65, no. 2, pp. 1074–1083, Feb. 2018.

[17] Y.-C. Kwon, J. Lee, and S.-K. Sul, "Recent advances in sensorless drive of interior permanent-magnet motor based on pulsating signal injection," *IEEE J. Emerg. Sel. Top. Power Electron.*, vol. 9, no. 6, pp. 6577–6588, Dec. 2021.

[18] M. Linke, R. Kennel, and J. Holtz, "Sensorless speed and position control of synchronous machines using alternating carrier injection," in *Proc. IEEE Int. Electric. Mach. Drives Conf.*, 2003.

[19] Y.-D. Yoon, S.-K. Sul, S. Morimoto, and K. Ide, "High-bandwidth sensorless algorithm for ac machines based on square-wave-type voltage injection," *IEEE Trans. Ind. Appl.*, vol. 47, no. 3, pp. 1361–1370, May/Jun. 2011.

[20] S. Kim, J.-I. Ha, and S.-K. Sul, "PWM switching frequency signal injection sensorless method in IPMSM," *IEEE Trans. Ind. Appl.*, vol. 48, no. 5, pp. 1576–1587, Sep./Oct. 2012.

[21] L. Chen, G. Gotting, and I. Hahn, "DC-link current and torque ripple optimized self-sensing control of interior permanent-magnet synchronous machines for hybrid and electrical vehicles," *IEEE Trans. Ind. Appl.*, vol. 53, no. 5, pp. 4536–4546, Sep./Oct. 2017.

[22] Z. Lin, Q. Geng, Z. Zhou, X. Li, and C. Xia, "MTPA control of sensorless IPMSM based on high frequency square-wave signal injection," in *Proc. IEEE Appl. Power Electron. Conf. Expo. (APEC)*. Anaheim, CA, USA: IEEE Press, 2019.

[23] Z. Lin, X. Li, Z. Wang, T. Shi, and C. Xia, "Minimization of additional high-frequency torque ripple for square-wave voltage injection IPMSM sensorless drives," *IEEE Trans. Power Electron.*, vol. 35, no. 12, pp. 13345–13355, Dec. 2020.
[24] C. Li, G. Wang, G. Zhang, N. Zhao, Y. Gao, and D. Xu, "Torque ripples minimization of sensorless SynRM drives for low-speed operation using Bi-HFSI scheme," *IEEE Trans. Ind. Electron.*, vol. 68, no. 7, pp. 5559–5570, Jul. 2021.
[25] M. Laumann, C. Weiner, and R. Kennel, "Arbitrary injection based sensorless control with a defined high frequency current ripple and reduced current and sound level harmonics," in *Proc. IEEE Int. Symp. Sensorless Control Elect. Drives (SLED)*, 2017.
[26] W. Li, M. Wu, X. Huang, and Z. Li, "Improved high frequency signal injection method based on fundamental current extraction for permanent magnetic synchronous motors," in *Proc. IEEE 30th Int. Symp. Ind. Electron. (ISIE)*, 2021.
[27] E. Armando, R. I. Bojoi, P. Guglielmi, G. Pellegrino, and M. Pastorelli, "Experimental identification of the magnetic model of synchronous machines," *IEEE Trans. Ind. Appl.*, vol. 49, no. 5, pp. 2116–2125, Sep./Oct. 2013.
[28] E. Armando, P. Guglielmi, G. Pellegrino, and R. Bojoi, "Flux linkage maps identification of synchronous AC motors under controlled thermal conditions," in *Proc. IEEE Int. Electr. Mach. Drives Conf. (IEMDC)*, 2017.
[29] M. Barcaro, M. Morandin, T. Pradella, N. Bianchi, and I. Furlan, "Iron saturation impact on high-frequency sensorless control of synchronous permanent-magnet motor," *IEEE Trans. Ind. Appl.*, vol. 53, no. 6, pp. 5470–5478, Nov./Dec. 2017.
[30] T. Tuovinen and M. Hinkkanen, "Adaptive full-order observer with high-frequency signal injection for synchronous reluctance motor drives," *IEEE J. Emerg. Sel. Top. Power Electr.*, vol. 2, no. 2, pp. 181–189, Jun. 2014.
[31] A. Yousefi-Talouki, P. Pescetto, and G. Pellegrino, "Sensorless direct flux vector control of synchronous reluctance motors including standstill, MTPA, and flux weakening," *IEEE Trans. Ind. Appl.*, vol. 53, no. 4, pp. 3598–3608, Jul./Aug. 2017.
[32] S. Buso and P. Mattavelli, *Digital Control in Power Electronics,* Morgan & Claypool, 2006.
[33] I. Bojoi, E. Armando, G. Pellegrino, and S. Rosu, "Self-commissioning of inverter nonlinear effects in ac drives," in *Proc. IEEE Int. Energy Conf. Exhib. (ENERGYCON)*, 2012.

András Holczer (Student Member, IEEE) was born in Siklós, Hungary. He received the B.Sc. (Hons.) degree in electrical engineering from Budapest University of Technology and Economics (BME), Budapest, Hungary, in 2019, and the M.Sc. (Hons.) degree in power engineering from Technical University of Munich (TUM), Munich, Germany, in 2021.

He was a Teaching Assistant with BME and TUM. Since 2021, he has been Industrial Ph.D. Student with Politecnico di Torino, Turin, Italy, and Huawei Nuremberg Research Center, Nuremberg, Germany.

Francisco D. Freijedo (Senior Member, IEEE) received the M.Sc. degree in physics from the University of Santiago de Compostela, Santiago de Compostela, Spain, in 2002, and the Ph.D. degree in electrical engineering from the University of Vigo, Vigo, Spain, in 2009.

From 2005 to 2011, he was a Lecturer with the Department of Electronics Technology, University of Vigo. From 2011 to 2014, he was with the Gamesa Innovation and Technology as a Power Electronics Control Engineer for renewable energy applications. From 2014 to 2016, he was a Postdoctoral Researcher with the Department of Energy Technology, Aalborg University, Aalborg, Denmark. From 2016 to 2019, he was a Scientific Collaborator with the Power Electronics Laboratory, Ecole Polytechnique Federale de Lausanne, Lausanne, Switzerland. He is currently with the Huawei Technologies, Nuremberg, Germany, as a Power Electronics Control Expert. His research interest includes power conversion technologies.

Dr. Freijedo is an Associate Editor for IEEE TRANSACTIONS ON INDUSTRIAL ELECTRONICS and IEEE TRANSACTIONS ON POWER ELECTRONICS.

Radu Bojoi (Fellow, IEEE) received the M.Sc. degree from Technical University of Iasi, Iasi, Romania, in 1993, and the Ph.D. degree from Politecnico di Torino, Torino, Italy, in 2002, both in electrical engineering.

He is a Full Professor in power electronics and electrical drives with the Energy Department G. Ferraris, and Head of the Power Electronics Innovation Center, Politecnico di Torino. He has authored or co-authored more than 200 papers covering electrical drives and power electronics for industrial applications, transportation electrification using wide-band gap power converters, power quality and grid stability improvement with power electronics, and home appliances. He has been involved in many research projects with industry for direct technology transfer aiming at obtaining new products.

Dr. Bojoi received the Nagamori Award in 2019 and he is the co-recipient of nine prize paper awards. He was a Co-Editor-In-Chief of the IEEE TRANSACTIONS ON INDUSTRIAL ELECTRONICS.